Biosensors and Bioelectronics 169 (2020) 112650

Contents lists available at ScienceDirect

Biosensors and Bioelectronics

journal homepage: http://www.elsevier.com/locate/bios

# A boosting upconversion luminescent resonance energy transfer and biomimetic periodic chip integrated CRISPR/Cas12a biosensor for functional DNA regulated transduction of non-nucleic acid targets

Cheng-Yu Li [a,*,1], Bei Zheng [b,1], Yu-Heng Liu [a], Jia-Ling Gao [a], Ming-Qiu Zheng [b], Dai-Wen Pang [c], Hong-Wu Tang [b,**]

[a] Hubei Province Key Laboratory of Occupational Hazard Identification and Control, School of Public Health, Medical College, Wuhan University of Science and Technology, Wuhan, 430065, People's Republic of China

[b] Key Laboratory of Analytical Chemistry for Biology and Medicine (Ministry of Education), College of Chemistry and Molecular Sciences, Wuhan University, Wuhan, 430072, People's Republic of China

[c] State Key Laboratory of Medicinal Chemical Biology, Tianjin Key Laboratory of Biosensing and Molecular Recognition, Research Center for Analytical Sciences, and College of Chemistry, Nankai University, Tianjin, 300071, People's Republic of China

ARTICLE INFO

*Keywords:*
Biomimetic chip
CRISPR/Cas12a
Functional DNA
Non-nucleic acid targets
Upconversion luminescence

ABSTRACT:

Apart from gene editing capacity, the newly discovered CRISPR/Cas systems offer an exciting option for biosensing field because of their excellent target recognition accuracy. However, the currently constructed sensors are not only limited to nucleic acid analysis but also suffer from poor adaptability in complex samples and unsatisfying sensitivity. We herein introduce some advanced concepts to break through these bottlenecks. First, the sensing targets are extended by skillfully designing a functional DNA such as aptamer (for protein) and DNAzyme (for metal ion) to regulate the transduction of non-nucleic acid species and further activate the *trans* cleavage of CRISPR/Cas12a. Second, a boosting upconversion luminescent resonance energy is triggered by using a peculiar energy-confining notion, whereby the luminescence domain is intensively restricted in a very narrow space (~2.44 nm) and up to 92.9% of the green emission can be quenched by the approaching BHQ-1 modified reporters. Third, a bio-inspired periodic arrangement biomimetic chip (photonic crystal) is employed to selectively reflect the upconversion luminescence to achieve noteworthy signal enhancement (~35-fold). By utilizing very simple detection devices (a 980 nm portable laser and a smartphone), the CRISPR/Cas12a biosensor shows commendable sensitivity and specificity toward model targets (ATP and $Na^+$, limits of detection are ~ 18 nM and ~0.37 μM, respectively). More importantly, the analysis of real complex samples demonstrate that the as-proposed platform can work as a powerful toolbox for monitoring the ATP fluctuation in single cell and point-of-care testing $Na^+$ in human plasma, enabling a broad application prospect.

## 1. Introduction

Most recently, the clustered regularly interspaced short palindromic repeats (CRISPR) based gene editing concept has attracted broad interests in biological and chemical sciences (Cong et al., 2013; English et al., 2019; Jinek et al., 2012; Palermo et al., 2017; Pardee et al., 2016). This revolutionary technology inspires from the adaptive immune response of bacteria and archaea towards invading viruses and such evolved foreign genetic cleavage endows the ability to artificially modify the endogenous genes for almost all kinds of organisms (Cong et al., 2013; Jinek et al., 2012). Because the associated nucleases (Cas proteins) need to be guided by a sequence of RNA (CrRNA), the precision of cleaving target DNA (*cis* cleavage) is significantly improved (Pardee et al., 2016). Compared with the early discovered CRISPR/Cas9 system, a newly developed Cas12a protein (a sort of type V nuclease) is not only capable of performing *cis* cleavage but also owns a unique feature for indiscriminately cleaving any non-specific single stranded DNA (*trans* cleavage) (Chen et al., 2018; Gootenberg et al., 2018). Profiting from the

* Corresponding author.
** Corresponding author.
*E-mail addresses:* li-chengyu@wust.edu.cn (C.-Y. Li), hwtang@whu.edu.cn (H.-W. Tang).
[1] Cheng-Yu Li and Bei Zheng contribute equally to this work.

https://doi.org/10.1016/j.bios.2020.112650
Received 13 August 2020; Received in revised form 15 September 2020; Accepted 22 September 2020
Available online 26 September 2020
0956-5663/

collateral cleavage, this powerful tool is extended to construct various biosensors such as electrochemistry (Dai et al., 2019), colorimetry (Chen et al., 2020; Hu et al., 2020) and fluorescence (Li et al., 2019b; Shan et al., 2019) to dramatically enhance the detection accuracy. Although much efforts have been made, nearly all of them are in the face of nucleic acid analysis. Very likely, the major difficulty lies in efficiently establishing a program that can transduce the identification events of non-nucleic acid targets into the activation of CRISPR/Cas12a (Xiong et al., 2020). Thus, resolving such limitation to move it forward is of urgent necessity.

Among the available CRISPR/Cas12a sensors, fluorescence means offers a better assay prospect because of its sensitive and stable signal readout (Fang et al., 2019). However, the current fluorescence acquisition modes are all based on the employment of traditional Stokes emission (visible light excitation), compelling them lack strong enough capabilities to work in complex samples (e.g. cell lysates and body fluids) (Li et al., 2018). Fortunately, a promising luminescent material that is upconverion nanoparticle (UCNP) is able to overcome this weakness (Li et al., 2020a; Wen et al., 2018; Zhang et al., 2019). Except for the splendid optical properties including very narrow half peak width (<20 nm) and admirable anti-photobleaching, the advantage of converting near-infrared (NIR) photons into visible ones can prominently degrease the biological background interference (Zhang et al., 2019). Particularly, selecting UCNP as the energy donor to establish luminescent resonance energy transfer (LRET) model to produce multiple optical information can further avoid false signals in practical application (Drees et al., 2016; Gao et al., 2019). Nevertheless, due to the relatively large size (>20 nm) of UCNP, the common energy acceptors such as fluorescent molecules (Drees et al., 2016; Muhr et al., 2017) and quenching substances (Gao et al. 2018, 2019bib_Gao_et_al_2019bib_Gao_et_al_2018; Wang et al., 2018) are hard to fall within the best space distance (<10 nm) even directly approaching the UCNP surface (Li et al., 2019a). Therefore, the resultant poor LRET efficiency (usually < 50%) caused by the invalid donors (the inside emitters) makes this favorable sensing option has a bottleneck in promoting sensitivity and it is desirable to find an effective improvement pathway.

Despite the introduction of upconversion LRET into CRISPR/Cas12a system is an innovative idea to reinforce anti-interference, another concern is the signal amplification on an approximate assay interface. Previous CRISPR/Cas12a sensors are generally conducted in homogeneous solutions, forcing them use a fluorometer to implement quantitative measurements. In practice, such large-scale platform is not a simple way for point-of-care testing (POCT), whereas the solid phase chip is a more feasible detection carrier. Inspiringly, abundant structural color materials in nature provide an interesting hint (Potyrailo et al., 2015; Yao et al., 2018; Zhao et al., 2012). For example, the regularly arranged flakes in the wings of Morpho butterfly endow a strong sunlight reflection phenomenon (Potyrailo et al., 2015). Based on this similar microscopic periodic structure of nature creatures, a variety of photonic materials are artificially fabricated to realize the selective interaction with light in a controllable manner. Among them, a kind of three-dimensional biomimetic nanostructure that is photonic crystal (PC) has aroused widespread attention (Hou et al., 2014; Wang et al., 2019). Generally, PC is formed by the self-assembly behavior of nanospheres without any fabricating equipment and its photonic band gap can be adjusted in a broad range by changing the size of the arrangement objects. Until now, many studies have demonstrated that PC can intensify the fluorescence reflection of plentiful materials including organic dyes (Li et al., 2020b) and quantum dots (Min et al., 2014), but the combination of PC and UCNP is rarely reported.

Following the above encouragements, here we for the first time propose a brand new CRISPR/Cas12a biosensor by integrating an energy-confining boosted upcoversion LRET with biomimetic interface assisted luminescence enhancement and apply it to perform the functional DNA regulated transduction of non-nucleic acid targets. As illustrated in Scheme 1, this artful sensor is principally composed of four components: (i) the programmed release of functional DNA locked activator under a non-nucleic acid target induced switching; (ii) the construction of boosting LRET process using an energy-confined UCNP as an energy donor; (iii) the collateral cleavage under the activation of CRISPR/Cas12a; (iv) the signal amplification and acquisition on a periodic arrangement biomimetic chip. Specifically, a functional DNA is first hybridized with the activator to perfectly achieve the locking effect and this silent activator is then opened to freely bind with the Cas12a-CrRNA complex *via* target transduction. Meanwhile, a novel polyacrylic acid (PAA) coated energy-confining UCNP with a sandwich

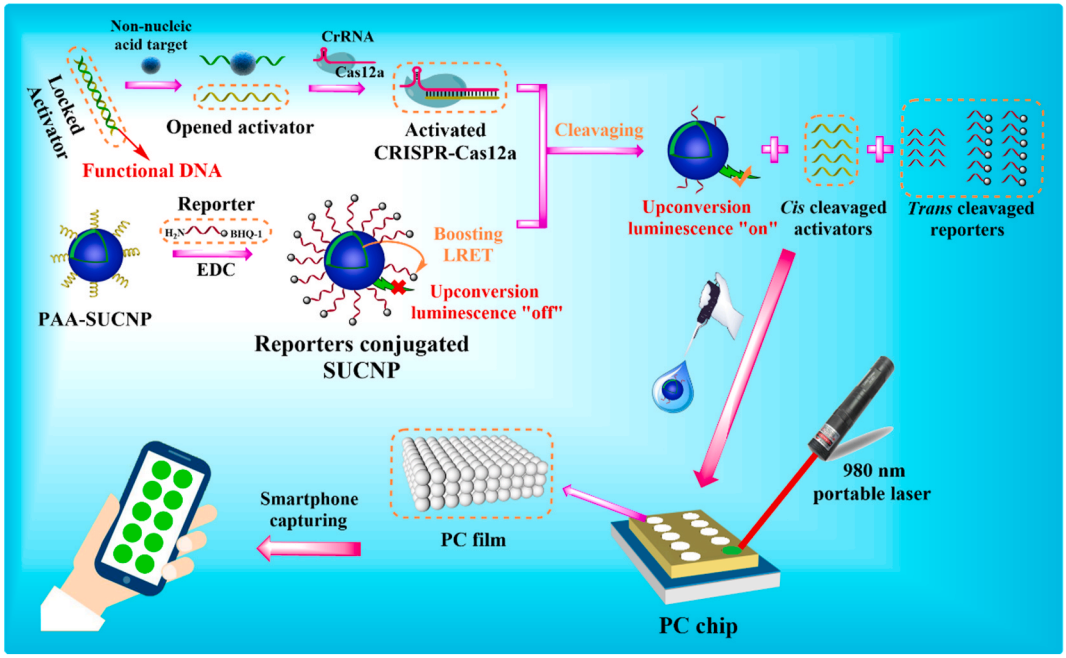


**Scheme 1.** Sensing principle (not to real scale) and workflow of the functional DNA regulated CRISPR/Cas12a biosensor for non-nucleic acid targets transduction by incorporating an energy-confining boosted upcoversion LRET with a biomimetic PC chip assisted luminescence amplification.

structure (SUCNP) is created and further covalently conjugated with a very short single stranded reporter (5 nt) modified with both BHQ-1 and amino group. Due to the proximity of pairing donor and acceptor, the upconversion luminescence is significantly quenched for a while. Under the enablement of activated *trans* cleavage of CRISPR/Cas12a, the surface attached reporters will be cleaved into fragments to keep away from the emission domain. By applying a 980 nm portable laser (~500 mW, detection device cost is only ~ 50 dollars) to irradiate the UCNPs loaded PC chip, the recovered upconversion luminescence image can be finally captured with a convenient smartphone.

## 2. Experimental section

### 2.1. Synthesis of oleic acid (OA)-Core ($NaYF_4$)

Initially, 1 mmol of $YCl_3{\cdot}6H_2O$ and a mixture containing 15 mL of 1-octadecene (ODE) and 6 mL of OA were mixed together in a 100 mL three-neck round-bottom flask for 10 min at room temperature. Then, vacuum treatment was processed to the flask for 40 min under vigorous stirring. Subsequently, the slurry was heated to 160 °C under high purity Ar flow and held the conditions for at least 40 min until it was turned into a clear yellowish solution. After the system is cooled to room temperature, 10 mL of methanol dissolving with $NH_4F$/NaOH (4 mmol/2.5 mmol, freshly prepared) was dropped carefully, followed by vigorous stirring for 30 min to obtain the oleate intermediates. Next, low boiling impurities as well as residual oxgen in the reaction were removed by degrassing the turbid white solution at 110 °C for 30 min. Upon performing again with the Ar protection, the flask temperature was quickly increased to 300 °C at a rate of 15 °C/min, and maintained the warm and gentle stirring for 60 min. To precipitate out and collect the products, the cooled golden yellow solution was first treated with 20 mL of ethanol and then centrifugated at 10,000 rpm for 6 min. Thereafter, the unreacted inorganic salts and organic solvents were removed by washing three times in turn with water/ethanol mixture (v/v = 1:1) and hexane/ethanol mixture (v/v = 1:6). Finally, the as-purified nanoparticles were handled with ultrasonic for 3 min in 8 mL of chloroform (concentration ~ 10 mg/mL) to form a homogeneous solution and stored at 4 °C for long-term storage.

### 2.2. Synthesis of OA-core-shell ($NaYF_4$@$NaYF_4$, Yb, Er)

A mixture of lanthanide chlorides (0.25 mmol) with a specific ratio (Y/Yb/Er = 0.8: 0.18: 0.02) was first fully stirred together with 10.5 mL of OA/ODE (v/v = 2:5) mixture in a 50 mL three-neck round-bottom flask and then performed with vacuum treatment for 40 min. After forming a transparent solution at 150 °C under Ar atmosphere, the flask was injected dropwise with the previously synthesized OA-Core solution, followed by orderly degassing at 110 °C for 20 min to remove the unnecessary chloroform and mixing with 5 mL of methanol containing $NH_4F$/NaOH (2 mmol/1.25 mmol, freshly prepared) for 30 min to obtain the slightly turbid oleate intermediates. By further degrassing the system at 110 °C for 30 min to evaporate off the needless methanol, it was allowed to heat to 300 °C under Ar flow and kept the reaction for 40 min. Upon treating the yellowish solution with excess ethanol, the precipitated nanoparticles were collected, washed and dispersed into 4 mL of chloroform (concentration ~ 20 mg/mL) for later use (stored at 4 °C).

### 2.3. Synthesis of OA-SUCNP ($NaYF_4$@$NaYF_4$, Yb, Er@$NaYF_4$)

First, a 50 mL three-neck round-bottom flask was added in sequence with 0.25 mmol of $YCl_3{\cdot}6H_2O$ and 10.5 mL of OA/ODE (v/v = 2:5) mixture. Next, the slurry was fully stirred and processed with vacuuming for 40 min, followed by heating to 160 °C and maintaining vigorous stirring to obtain a clear solution under Ar flow. Subsequently, the earlier synthesized OA-Core-Shell solution was injected dropwise into the flask and then treated with degassing at 110 °C for 20 min. Upon vigorous stirring with 5 mL of methanol containing $NH_4F$/NaOH (2 mmol/1.25 mmol, freshly prepared) for 30 min, the slightly turbid solution was further degassed at 110 °C for 30 min. Then, the system temperature was raised to 300 °C in 20 min and keeping the temperature for 40 min. After precipitating, collecting and washing the products, the resultant nanoparticles were dealt with ultrasonic in 4 mL of chloroform (concentration ~ 20 mg/mL) for at least 10 min and stored at 4 °C for later use. For this synthetic pathway, the thickness of outer shell can be controllably regulated by introducing different ratios of OA/ODE.

## 3. Results and discussion

### 3.1. Synthetic pathway and characterization of energy-confining UCNP

As shown in Fig. 1A, a routine seed-mediated growth strategy (Guo et al., 2010) is employed to create the peculiar energy-confining UCNP layer-by-layer. With regard to this sandwich structure design, all the OA capped hydrophobic layers are constructed by thermally decomposing rare earth chloride precursors at 300 °C. Specifically, $NaYF_4$ nanoparticle is first prepared as the host core alone and then the pairing sensitizers/activators (Yb/Er: 18%/2%) are narrowly distributed in another extended $NaYF_4$ inner shell with an extremely thin layer (~2.5 nm). To prevent the luminescence quenching of such emission domain, a crucial $NaYF_4$ outer shell is further deposited on the core-shell case. On account of the demand of hydrophilic surface to conjugate biomolecules, a simple ligand exchange approach at liquid-liquid interface (260 °C) (Sedlmeier and Gorris, 2015) is finally implemented to replace the primary OA molecules with PAA polymers.

The as-proposed crystal growth process is expressly demonstrated by a sequence of transmission electron microscopy (TEM) images (Fig. 1B–D), from which spherical forms are well maintained for all the nanostructures and no agglomerations occur to the shell development. Of note, the altered ligand does not affect the morphology and the monodispersity (Fig. 1E). Relevant counting histograms (Figs. S1A–S2C) clearly display the size evolution, where the hydrophobic nanoparticles are gradually broadened within very small ranges of deviations ($\sigma < 5\%$, $n = 400$) and the mean diameter for each case is 28.52 nm (OA-Core, $NaYF_4$), 30.96 nm (OA-Core-Shell, $NaYF_4$@$NaYF_4$, Yb, Er), 33.31 nm (OA-SUCNP, $NaYF_4$@$NaYF_4$, Yb, Er@$NaYF_4$), respectively, and no pronounced variation presents to PAA-SUCNP (33.41 ± 1.27 nm, Fig. S1D), also suggesting the good stability of crystal progress. High-resolution TEM images (Figs. S2A–S2C) exhibit obvious single crystal properties for all cases and their lattice fringe spacings are determined as 5.2 Å, corresponding to the hexagonal direction index ([101(_)0]) of β-$NaYF_4$. X-ray diffraction (XRD) patterns (Fig. 1F) further verify these highly crystallized regions, among which the featured diffraction lines are entirely in accordance with the standard β-$NaYF_4$ (JCPDs: 28–1192) and no other impurities appear, along with indicating the crystal completeness of this synthetic pathway. Energy dispersive spectrum (EDS, Fig. 1G) analyses manifest the definite doping rare earth elements in each layer, whereby the inner shell is assuredly concentrated with the emitters ($Er^{3+}$). The noteworthy symmetric/antisymmetric (1557 $cm^{-1}$/1464 $cm^{-1}$) vibration of carboxylate anions together with the asymmetrical long alkyl chain stretching (2924 $cm^{-1}$) assigned in Fourier transform infrared (FT-IR) spectra (Fig. 1H, **three bottom lines**) prove the surface OA capping during the size increasement and this non-polar sustaining leads to good solubilities in chloroforms (Figs. S3A–S3C), while significant attenuation of these typical OA bands comes to PAA-SUCNP (Fig. 1H, **top line**) and results in the formation of a homogeneous aqueous solution (Fig. S3D).

Once these solutions are irradiated by a 980 nm continuous wave laser, it can be found that the luminescence peak around 543 nm ($^4S_{3/2} \rightarrow {}^4I_{15/2}$ of $Er^{3+}$, Drees et al., 2016, Fig. S4) is observably enhanced by 3.77-fold by virtue of the introduction of outer shell (Fig. 1I, **blue and green lines**). Although such green emission is decreased by ~25% due

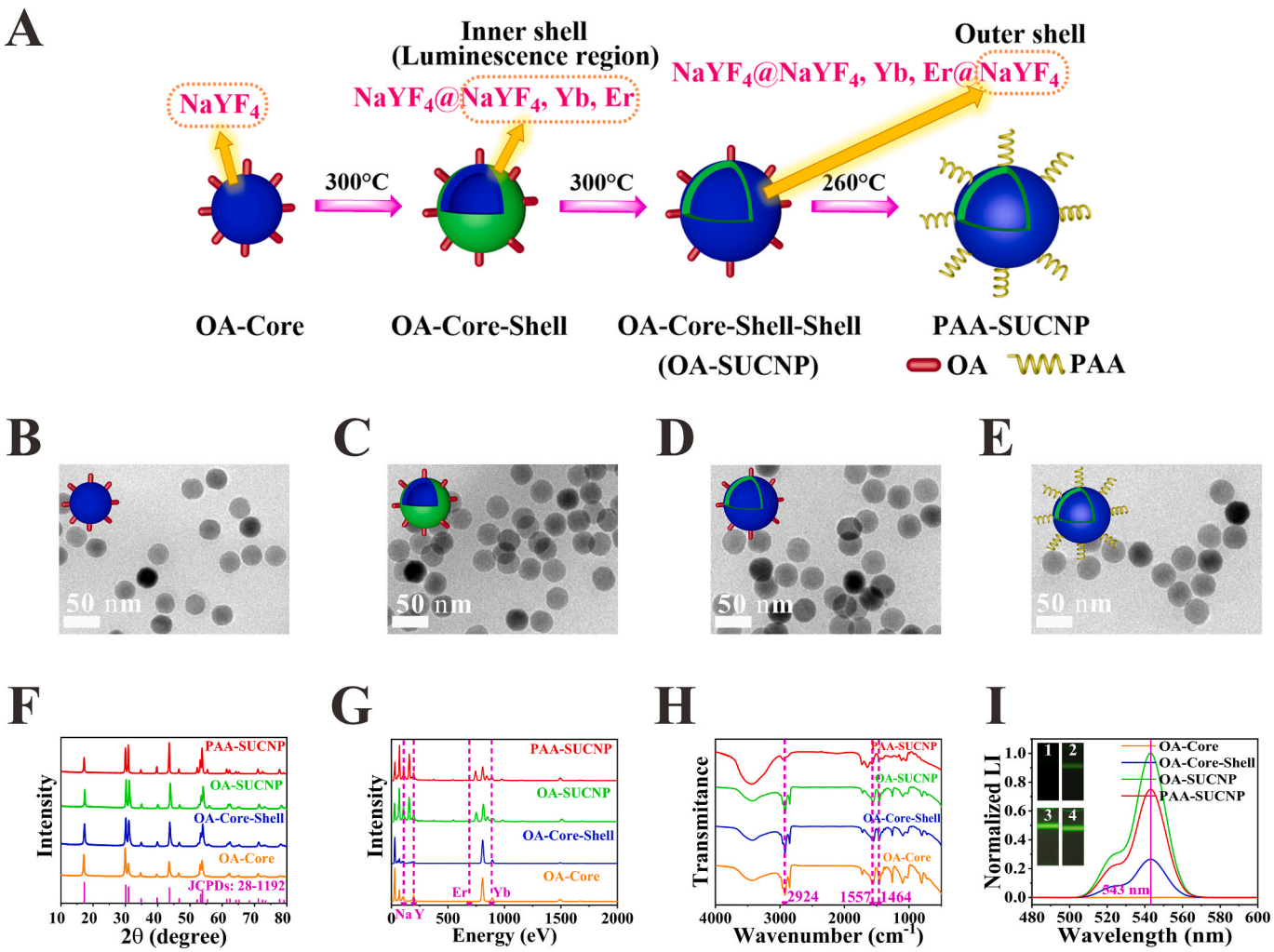


**Fig. 1.** (A) Synthetic pathway (not to real scale) of OA capped energy-confining UCNP with a sandwich structure through a seed-mediated growth route layer-by-layer and its surface PAA coating *via* a ligand exchange strategy. (B)–(D) TEM images of the prepared UCNPs with the structures of core (OA-Core, $NaYF_4$), core-shell (OA-Core-Shell, $NaYF_4$@$NaYF_4$, Yb, Er) and core-shell-shell (OA-SUCNP, $NaYF_4$@$NaYF_4$, Yb, Er@$NaYF_4$), respectively. (E) TEM image of PAA-SUCNP. Scale bars are 50 nm for all cases. (F)–(H) XRD patterns, EDS lines, FT-IR spectra of these nanostructures. (I) Upconverion luminescence spectra of the nanoparticles dispersed in corresponding solvents. Inset: digital images under the irradiation of a 980 nm portable laser (laser power ~ 500 mW, numbers 1–4: OA-Core, OA-Core-shell, OA-SUCNP, PAA-SUCNP).

to the non-radiative relaxation in water environment (Fig. 1I, **red line**), the optical (Fig. S5A) and colloidal (Fig. S5B) nature of PAA-SUCNP are finely held within 60 days of storage, laying a favorable basic for conducting bioconjugation. After conjugating the reporters through 1-(3-dimethylaminopropyl) -3-ethyl carbon diamine (EDC) chemistry, not only the hydration layer is thickened by ~ 2 nm (Fig. S6A) but also possessing more negative charges (from −22.6 to −30.7 mV, Fig. S6B). Besides, a highly efficient conjugation event is testified by the negligible absorbance at 260 nm belonging to the characteristic absorption of nucleic acids (Gabelica et al., 2007) for the reaction supernatant (Fig. S6C).

### 3.2. Fabrication procedures and characterization of PC chip

Fig. 2A illustrates the fabrication procedures of PC chip. In detail, the cleaned cover glass is first silanized to turn its surface into hydrophobic and then coated with a layer of polydimethylsiloxane (PDMS) film (~3 mm) punched with ten hollow holes (~5 mm in diameter). After that, carboxyl polystyrene sphere (PS, size ~ 240 nm) droplets are added into these holes and allow them evaporate naturally at 37 °C. Such series of surface modification is certified by contact angle test (Fig. 2B), among which the contact angle is 110° after the silanization, whereas it becomes less than 10° when depositing the monodispersed PSs, revealing the construction of a hydrophilic interface. Plane scanning electron microscopy (SEM) image (Fig. 2C) manifests that the evaporated PSs appear a unique self-assembly behavior, whereby a closely packed and highly ordered periodic arrangement is formed on the PDMS film, and the cross-section image (Fig. 2D) provides a multilayer distribution feature. Transmittance spectra (Fig. 2E, **red line**) visibly explains that the coverage of photonic band gap is from 500 to 580 nm and the maximal value locates around 540 nm, endowing a strong green light reflection ability under sunlight due to the Bragg scattering effect (Fig. 2E, **inset**). Beyond that, this special selectivity will not be influenced by the surface loaded PAA-SUCNPs (Fig. 2E, **blue line**).

### 3.3. Investigation of luminescence enhancement on PC film

Before establishing the CRISPR/Cas12a biosensor, it is necessary to investigate two essential issues. On one hand, the practical signal enhancement capability is a key prerequisite for luminescence-based detection to improve sensitivity. For this reason, we tentatively compare three different luminescent materials including carboxyfluorescein (FAM), 5-carboxytetramethylrhodamine (TAMRA), N,N′-(dipropyl)-tetramethyl-indodicarbocyanine (Cy5) with PAA-SUCNP on

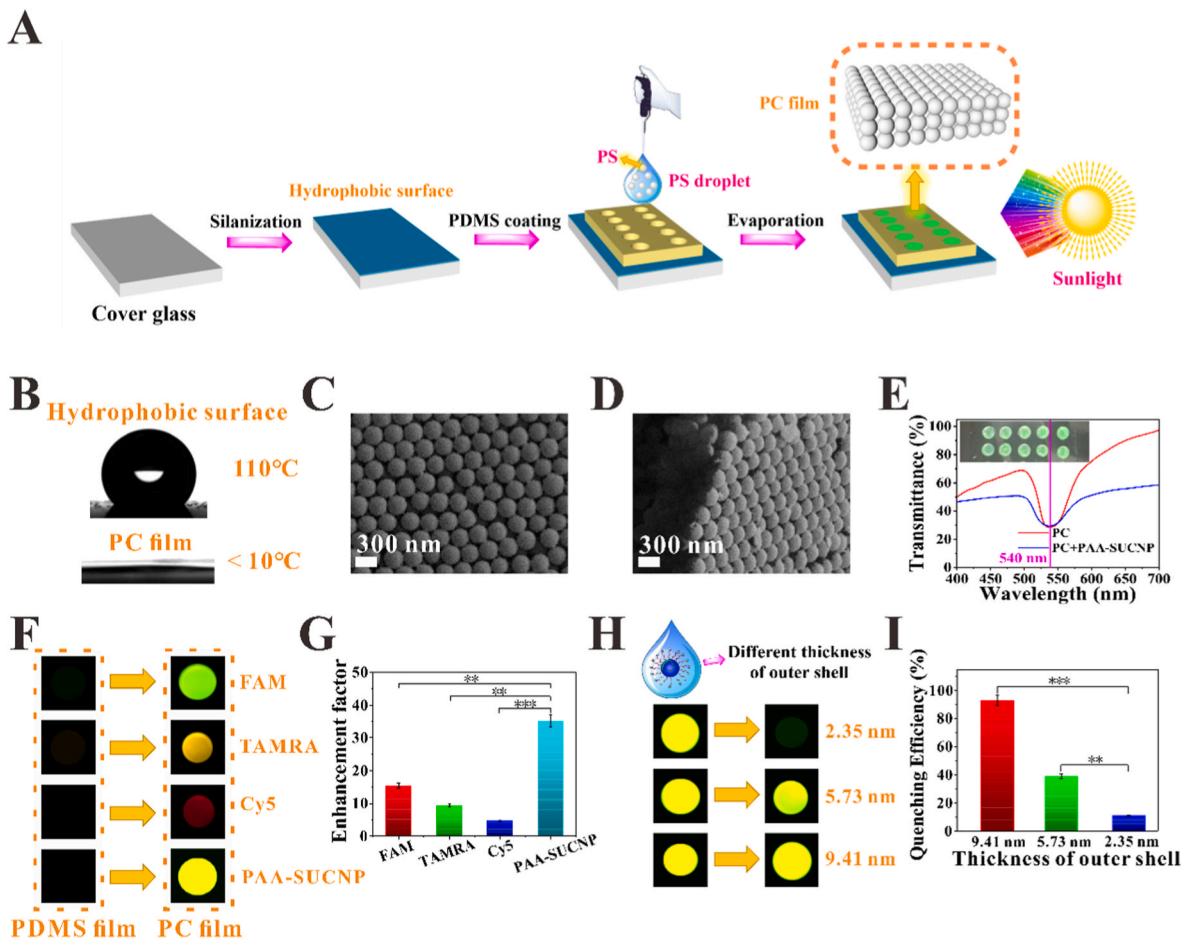


**Fig. 2.** (A) Fabrication procedures (not to real scale) of PC chip. (B) Contact angle test of surface modification. (C) Plane SEM image of PC film. (D) Cross-section SEM image of PC film. Scale bars are 300 nm for cases. (E) Transmittance spectra of PC film and PAA-SUCNPs loaded PC film. Inset: real digital image of PC chip under sunlight. (F) Fluorescence images (captured under the corresponding optimal excitation sources) of PDMS films (left) and PC films (right) loaded with FAM, TAMRA, Cy5 and PAA-SUCNP. (G) Enhancement factor of PC film quantified from (F). (H) Upconversion luminescence images of PC films loaded with PAA-SUCNPs possessing different thickness of outer shells (2.35, 5.73, 9.41 nm) before and after conjugating with BHQ-1 modified reporters. (I) Quenching efficiency calculated from (H). $^{**}P < 0.01$, $^{***}P < 0.001$.

PDMS and PC films. In Fig. 1F, under the optimal excitation sources and low concentration conditions (~1 nM), very weak brightness happen to all the PDMS films and the PAA-SUCNPs loaded PC film presents the strongest emission intensity owing to the perfect overlap between the upconversion luminescence spectrum and the photonic band gap. According to the quantitative measurements (Fig. 2G), we can also acquire that the exact enhancement factor for PAA-SUCNP is as high as 35.2 while progressively dropped to 15.4, 9.3, 4.6 for FAM, TAMRA, Cy5, respectively. Moreover, although the PC chip cannot be reused due to the nonspecific adsorption between the PC film and the UCNP, it shows no visible difference between batches and within batches (Fig. S13). These results confirm that the PC chip is an ideal and reliable choice to achieve signal amplification.

### 3.4. Exploring the optimal LRET efficiency on PC film

On the other hand, despite of the fact that the upconversion luminescence can be restrictedly excited into the inner shell with only 2.44 nm for the sandwich structure, the thickness of outer shell can cause different space distance to energy acceptor and thus intensively impacts the LRET efficiency (the thinner outer shell, the better LERT effect). To inspect this inference, we keep the core-shell sizes (30.96 nm) and synthesize additional OA-SUCNPs with thicker outer shells. According to the Ostwald ripening theory, the number of surface ligands can directly determine the crystal sizes (Gnanasammandhan et al., 2016). Hence, another two types of sandwich cases with the mean sizes of 36.69 nm (Fig. S7) and 40.37 nm (Fig. S8) are obtained by varying the ratios of OA and ODE to 3:4 and 4:3, respectively. For this size tuning means, both the crystal nature (Fig. S9) and the hydrophobic surfaces (Fig. S10) are maintained pretty well. After performing the ligand exchanging for these larger nanoparticles (Figs. S11 and S12) and conjugating the reporters to construct the LRET model, the corresponding quenching ability of BHQ-1 to upconversion luminescence is evaluated on PC film. Notably, the sharp decline of luminescence lifetime (Fig. S14) for acceptors attached PAA-SUCNP mightily attests that the anticipant non-radiation transition process is actually triggered and the concentration of conjugated reporters can observably affect the quenching efficiency (Fig. S15). In comparison with the extremely high quenching efficiency (~92.9%) for 2.35 nm of outer shell (the size of OA-SUCNP is 33.31 nm from the beginning prepared), the increased outer shells give rise to apparently weaker energy transfer effect, i.e., 39.2% and 11.4% for 5.73 nm and 9.41 nm cases, respectively (Fig. 2H and I), enabling a controllable way to implement the confinement conception.

### 3.5. Sensing principle and performance toward standard ATP in buffer solution

With the assistance of the above conclusive foundations, we start to put forward the CRISPR/Cas12a based sensing modes for non-nucleic acid targets. To begin with, the most widespread energy currency in

living organisms (Adenosine 5′-triphosphate, ATP) (Tsujimoto, 1997; Qu et al., 2018; Ratajczak et al., 2019) is selected as the on-site transducer (model target). Fig. 3A uncovers the target switching principle, by which the activator chain is first completely locked by two ATP-specific aptamers (Xiong et al., 2020) acting as the functional DNAs *via* an annealing treatment and then released from the hybridization structure in the presence of ATP by reason of the high affinity binding caused conformational change. Meanwhile, the *trans* cleavage activity of CrRNA guided Cas12a is effectively initiated due to the recognition of the opened activator. Such aptamer induced process is then investigated by the upconversion luminescence study for the reporters conjugated PAA-SUCNP. It can be seen from Fig. 3B that minimal luminescence signal arises to the absence of pure activator (also for the locked activator) while a considerable luminescence recovery is exhibited to the target group (ATP ~ 1 mM). To further corroborate this finding, we attempt the indiscriminate cleavage ability towards a FAM labeled single stranded DNA (ssDNA-FAM) substrate with 21 nt. The agarose gel electrophoresis result (Fig. 3C) indicates that the substrate is availably cleaved into random short fragments when using ATP to open the activator and this degradation phenomenon is quite similar to the normal CRISPR/Cas12a system, whereas no cleavage effect happens to the locked activator.

After introducing different amounts of ATP to the sensing frame and conducting the signal readout on PC chip under the optimal conditions (e.g., reaction time ~ 15 min, pH ~ 8.0, temperature ~ 37 °C, Fig. S16), it comes to a follow that the luminescence recovery sign vastly depends on the target concentration ranging from 30 nM to 100 μM (Fig. 3D, **top image**). On the contrary, without the luminescence enhancement of PC, no eyeable difference between the detected signals and the blank group is observed (Fig. 3D, **bottom image**). By accurately quantifying the brightness of these images through the Image-J software, it is obtained that the relative luminescence intensity ($(F–F_0)/F_0$, where F and $F_0$ represents the luminescence intensity in the presence and absence of ATP, respectively) increases linearly ($R^2$: 0.9968) with the logarithm of the target concentration crossing four orders of magnitude (Fig. 1E). In the light of 3σ/slope criterion (where σ indicates the standard deviation of seven blank group signals), the limit of detection (LOD) is calculated to be as low as 18 nM, a superior assay performance to the conventional ATP kit (LOD ~ 1 μM) and other advanced optical sensors (Table S2).

In addition to sensitivity, the specificity is next systematically examined by applying the sensing strategy to respond three nucleotide-triphosphate analogues including (guanosine triphosphate) GTP, (cytidine triphosphate) CTP and (uridine triphosphate) UTP, three non-specific proteins such as bovine serum albumin (BSA), carcinoembryonic antigen (CEA) and alpha fetal protein (AFP) as well as random nucleic acids (DNA and RNA). As displayed in Fig. 1F, the introduction of target can produce the most conspicuous signal recovery ($p < 0.001$). Among the competitive analogues, even if their concentrations (500 μM) are 5-fold higher than ATP, the acquired luminescence intensities are slightly higher than the blank signal ($p < 0.05$) and they accounts for only ~13% against the target signal by taking the advantage of the highly specific binding instinct of aptamer. For the latter two cases, the non-analogues (even at 1000 μM) can hardly in favor of restoring the quenched luminescence and such weak intensities show no significant difference ($p > 0.05$) to the blank group. As a result, our careful inspection suggests an outstanding specificity towards ATP detection.

### 3.6. Sensing principle and performance toward standard $Na^+$ in buffer solution

Motivated by the successful ATP analysis, we subsequently extend this sensing methodology to $Na^+$ testing (also model target) to validate its generality. In Fig. 4A, a $Na^+$-fueled DNAzyme frame (Xiong et al., 2020) working as the functional DNA is employed to flexibly open the activator. Concretely, the right binding arm of DNAzyme is designed to perfectly complement to the activator which simultaneously serves as the catalytic substrate. Upon embedding $Na^+$ into the loop structure, the $Na^+$ fueled catalytic reaction will cleave the substrate strand (Chen et al., 2020) to release the activator and it will be further bound to the Cas12a-CrRNA complex. Similarly, such DNAzyme regulated *trans* cleavage effect is concurrently demonstrated by the upconversion luminescence study (Fig. 4B) and the electrophoresis experiment

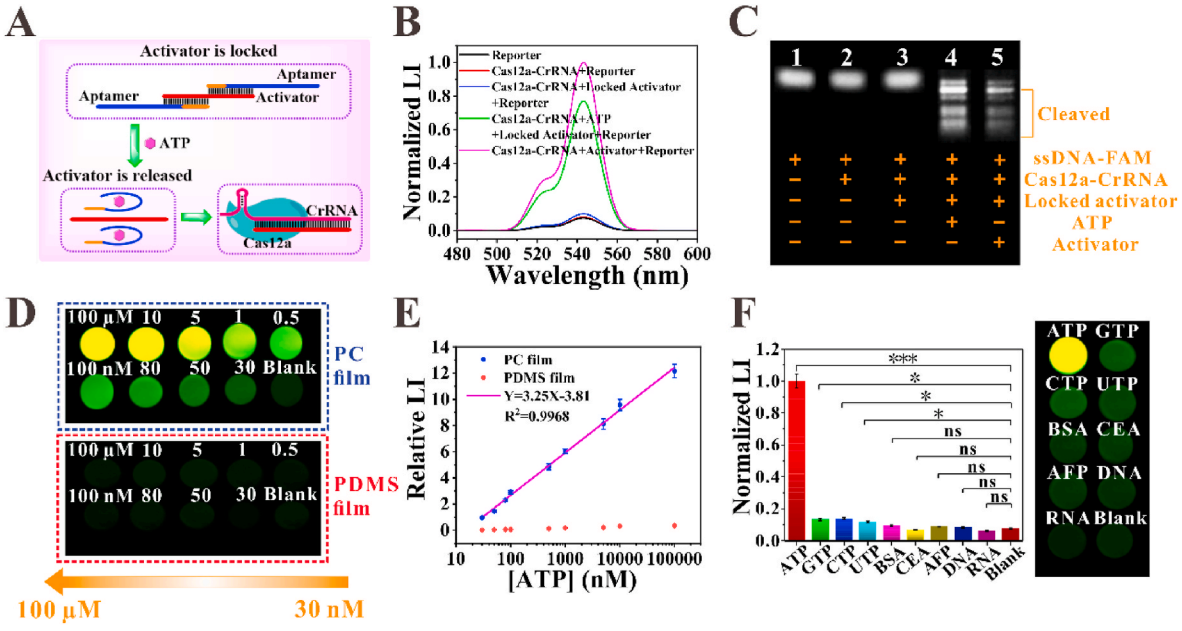


**Fig. 3.** (A) Schematic illustration (not to real scale) of CRISPR/Cas12a activation by aptamer regulation. (B) Upconversion luminescence study of the aptamer regulated CRISPR/Cas12a biosensor (the *trans* cleavage is for reporters conjugated PAA-SUCNP). (C) Agarose gel electrophoresis analysis of the aptamer regulated CRISPR/Cas12a biosensor (the *trans* cleavage is for ssDNA-FAM). (D) Upconversion luminescence images in the introduction of different amounts of ATP (30 nM–100 μM) on PC (up) and PDMS films (bottom). (E) Linear relationship between the relative luminescence intensity ($(F–F_0)/F_0$) and the logarithm of ATP concentration on PC and PDMS films measured from (D) *via* the Image-J software. (F) Specificity examination of ATP detection towards GTP, CTP, UTP, BSA, CEA, AFP, DNA and RNA. *$P < 0.05$, ***$P < 0.001$, ns: no significant difference ($p > 0.05$).

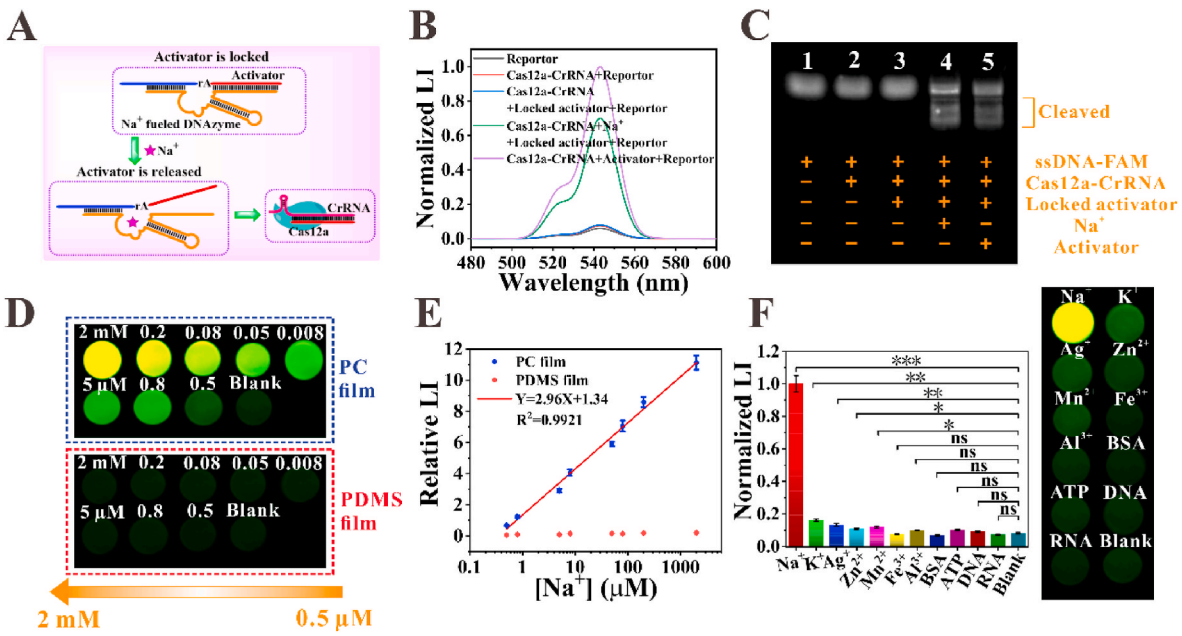


**Fig. 4.** (A) Schematic illustration (not to real scale) of CRISPR/Cas12a activation by $Na^+$-fueled DNAzyme regulation. (B) Upconversion luminescence study of the DNAzyme regulated CRISPR/Cas12a biosensor (the *trans* cleavage is for reporters conjugated PAA-SUCNP). (C) Agarose gel electrophoresis analysis of the DNAzyme regulated CRISPR/Cas12a biosensor (the *trans* cleavage is for ssDNA-FAM). (D) Upconversion luminescence images in the introduction of different amounts of $Na^+$ (0.5 μM–2 mM) on PC (up) and PDMS films (bottom). (E) Linear relationship between the relative luminescence intensity ($(F–F_0)/F_0$) and the logarithm of $Na^+$ concentration on PC and PDMS films measured from (D) *via* the Image-J software. (F) Specificity examination of $Na^+$ testing towards $K^+$, $Ag^+$, $Zn^{2+}$, $Mn^{2+}$, $Fe^{3+}$, $Al^{3+}$, BSA, ATP, DNA and RNA. $^*P < 0.05$, $^{**}P < 0.01$, $^{***}P < 0.001$, ns: no significant difference ($p > 0.05$).

(Fig. 4C) as well. Moreover, in the concentration range of 0.5 μM–2 mM, the sensing system shows poor responsiveness on PDMS film (Fig. 4D, **bottom image**) while a distinct luminescence recovery trend gives rise to the PC film (Fig. 4D, **top image**). Following the same intensity statistics, it also comes to a strictly linear curve ($R^2$: 0.9921, Fig. 4E) and the LOD is estimated low to 0.37 μM, a preeminent analytical ability compared to the traditional $Na^+$ meter (LOD ~ 1 mM) and the current luminescence-based detection strategies (Table S3). Most importantly, thanks to the high affinity of DNAzyme, no matter it is a non-target metal ion or a biomolecule, the sensing approach can maintain excellent specificity (Fig. 4F).

### 3.7. Sensing ability towards ATP in single cell

As the indispensable carrier of energy conversion, ATP plays a vital role in various cellular processes such as division, proliferation and differentiation, making it can serve as a useful indicator for reflecting the metabolic activity of viable cells (Tsujimoto, 1997).Therefore, the detection of intracellular ATP, especially in single cell, is of great importance. Benefitting from the exciting LOD, we finally explore the newly developed sensing method to fulfill this goal. In this experiment, the adherent cells (~$10^4$) is first digested to the suspension states and then lysed to extract the inner total proteins and nucleic acids (Fig. 5A). Considering the intracellular ATP concentration (1–10 mM) (Hong et al., 2020), the extractives need to be further diluted to fall within this window. Based on the as-gained linear relationship, we quantitatively analyze three kinds of cancer cells (MCF-7, HeLa, A549) and one normal cell (T). In Fig. 5B, the evaluated ATP levels in these single cells are 4.4 (MCF-7), 1.6 (HeLa), 2.7 (A549), 3.2 mM (T), respectively, matching well with the values determined from the commercial colorimetric kit ($p > 0.05$). Such delicate difference is also confirmed by other reports (Hong et al., 2020; Wang et al., 2020) and it can be mainly attributed to the higher glucose uptake to compensate for the anaerobic respiration of cancer cells. Furthermore, monitoring the ATP fluctuation in single MCF-7 cell is performed. In our design, $CaCl_2$ (5 mM) and oligomycin (10 μM, a type of ATPase inhibitor, Ratajczak et al., 2019) are utilized as the modulation media for up-regulating and decreasing the ATP levels, respectively. The results (Fig. 5C) display that the $CaCl_2$ treated group increases to 6.6 mM/cell while the down-regulated group reduces to 2.1 mM/cell.

### 3.8. Sensing ability towards $Na^+$ in human plasmas

As is well-known, $Na^+$ is an important inorganic element in human body and it participates the water metabolism to balance the osmotic pressure and pH in body fluids (Kovacs and Robertson, 1992; Simpson, 1988). Clinically, the normal plasma $Na^+$ is kept from 135 to 145 mM and its deficiency (<135 mM, termed as hyponatremia) can cause diverse symptoms including weakness, emesis and headache (Simpson, 1988). The frequently-used $Na^+$ selective electrode ($Na^+$ meter) is easily influenced by the environmental disturbance (Megahed et al., 2019). Thus, it is critical to develop a more reliable means to meet the clinical requirement. To this end, our method is exploited to test $Na^+$ contents in real human plasma samples (approved by the Ethical Committee of Wuhan University of Science and Technology Hospital). Before performing this task, the potential interference signals (e.g. autofluorescence and scattering light) derived from the complicated matrices in this challenging medium must be inspected. Satisfactorily, owing to the anti-Stokes luminescence associated with the converting of NIR photons (Li et al., 2020a), both the signal-to-background ratio (as high as ~ 26, Fig. S17A) and the working curve (Fig. S17B) do not emerge noticeable changes even in whole plasma. For actual operation, the collected venous bloods containing 1% heparin (whole blood) are first centrifuged to obtain the yellowish plasmas (whole plasma, Fig. 5D) and then diluted 100-fold. In the same way, we detected 15 hyponatremia patients and 10 healthy donors, and the assay results present a strong positive correlation to that of $Na^+$ meter ($p > 0.05$, Fig. 5E), demonstrating a benign accuracy and POCT capacity in complex samples.

## 4. Conclusion

In consequence, this study presents a general and versatile CRISPR/

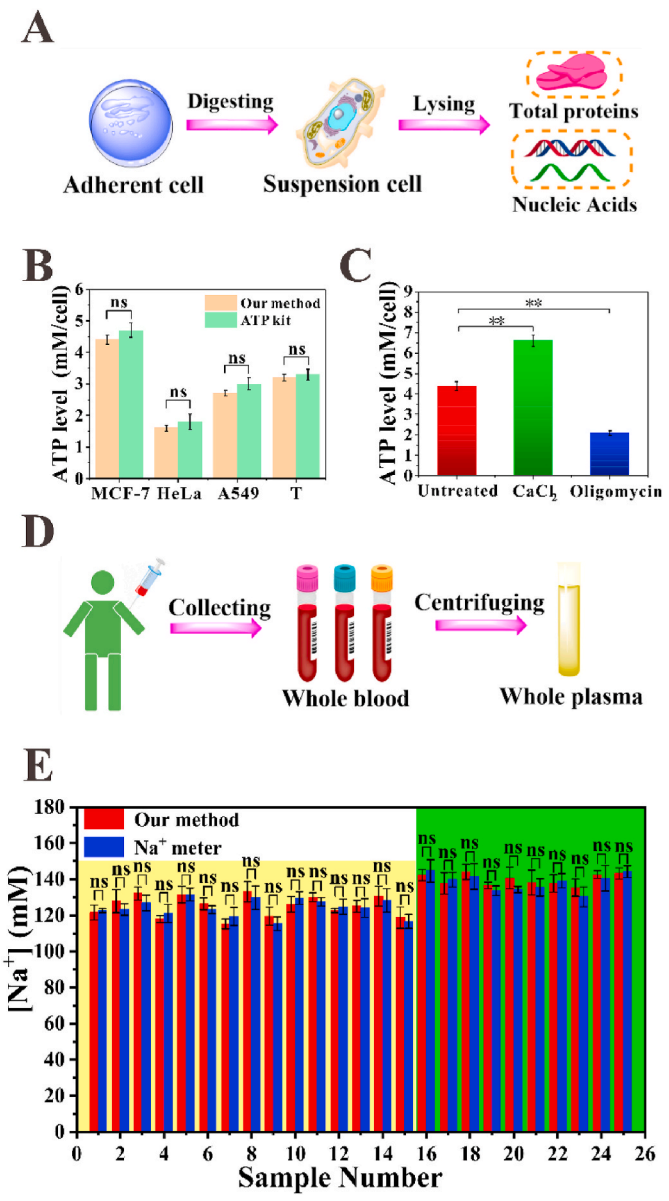


**Fig. 5.** (A) Operation steps (not to real scale) of cell lysates extraction. (B) Comparison of ATP levels in single MCF-7, HeLa, A549 and T cell between our method and commercial colorimetric kit. (C) Monitoring results of ATP fluctuation in a single MCF-7 cell by treating with $CaCl_2$ (up-regulation reagent) and oligomycin (down-regulation reagent), respectively. (D) Operation steps (not to real scale) of human whole plasma extraction. (E) Comparison of $Na^+$ contents in 20 cases of human plasmas between our method and traditional $Na^+$ meter. Yellow and Green regions represent hyponatremia patients and healthy donors, respectively. $^{**}P < 0.01$, ns: no significant difference ($p > 0.05$). (For interpretation of the references to color in this figure legend, the reader is referred to the Web version of this article.)

Cas12a biosensor by combining a functional DNA regulated target transduction, an energy-confining boosted upcoversion LRET with a biomimetic chip assisted signal amplification. By separately utilizing aptamer and DNAzyme as the switching media, the CRISPR/Cas12a system can be activated by specifically recognizing the model targets (ATP and $Na^+$) to trigger the programmed collateral cleavage of Cas12a-CrRNA. The innovative energy-confining design successfully engineers a sandwich structured UCNP by restricting the emission region into a very limited space scope (2.44 nm), allowing not only an impressive LRET efficiency (~92.9%) to the surface conjugated BHQ-1 modified reporters but also a solid way for analysis of complex samples. Upon loading the *trans* cleaved products onto a periodically arranged PC chip, the perfectly matched photonic band gap remarkably enhances the upconversion luminescence to approximately 35-fold, resulting in an ultrasensitive assay performance toward the representative small molecules (LOD ~ 18 nM for ATP, LOD ~ 0.37 μM for $Na^+$). In particular, the quite favorable response abilities toward single cell and human plasma pave a new venue for clinical diagnosis.

## CRediT authorship contribution statement

**Cheng-Yu Li:** Conceptualization, Methodology, Validation, Investigation, Writing - original draft, Writing - review & editing, Visualization, Supervision, Project administration, Funding acquisition. **Bei Zheng:** Methodology, Validation. **Yu-Heng Liu:** Validation, Investigation. **Jia-Ling Gao:** Validation, Investigation. **Ming-Qiu Zheng:** Validation, Investigation. **Dai-Wen Pang:** Writing - review & editing, Project administration. **Hong-Wu Tang:** Conceptualization, Methodology, Writing - original draft, Writing - review & editing, Visualization, Supervision, Project administration, Funding acquisition.

## Declaration of competing interest

The authors declare that they have no known competing financial interests or personal relationships that could have appeared to influence the work reported in this paper.

## Acknowledgments

This work was supported by the National Natural Science Foundation of China (21904102, 81772256 and 21827808).

## Appendix A. Supplementary data

Supplementary data to this article can be found online at https://doi.org/10.1016/j.bios.2020.112650.

## References

Chen, J.S., Ma, E.B., Harrington, L.B., Da Costa, M., Tian, X.R., Palefsky, J.M., Doudna, J. A., 2018. Science 360 (6387), 436–439.
Chen, K., Huang, Q., Fu, T., Ke, G.L., Zhao, Z.B., Zhang, X.B., Tan, W.H., 2020a. Anal. Chem. 92 (11), 7404–7408.
Chen, Q., Tian, T., Xiong, E.H., Wang, P., Zhou, X.M., 2020b. Anal. Chem. 92 (1), 573–577.
Cong, L., Ran, F.A., Cox, D., Lin, S.L., Barretto, R., Habib, N., Hsu, P.D., Wu, X.B., Jiang, W.Y., Marraffini, L.A., Zhang, F., 2013. Science 339 (6121), 819–823.
Dai, Y.F., Somoza, R.A., Wang, L., Welter, J.F., Li, Y., Caplan, A.I., Liu, C.C., 2019. Angew. Chem. Int. Ed. 58 (48), 17399–17405.
Drees, C., Raj, A.N., Kurre, R., Busch, K.B., Haase, M., Piehler, J., 2016. Angew. Chem. Int. Ed. 55 (38), 11668–11672.
English, M.A., Soenksen, L.R., Gayet, R.V., de Puig, H., Angenent-Mari, N.M., Mao, A.S., Nguyen, P.Q., Collins, J.J., 2019. Science 365 (6455), 780–785.
Fang, X.N., Zheng, Y.Z., Duan, Y.K., Liu, Y., Zhong, W.W., 2019. Anal. Chem. 91 (1), 482–504.
Gabelica, V., Rosu, F., Tabarin, T., Kinet, C., Antoine, R., Broyer, M., De Pauw, E., Dugourd, P., 2007. J. Am. Chem. Soc. 129 (15), 4706–4713.
Gao, M.P., Wu, R.Y., Mei, Q.S., Zhang, C.L., Ling, X., Deng, S.S., He, H.B., Zhang, Y., 2019. ACS Sens. 4 (11), 2864–2868.
Gao, R., Hao, C.L., Xu, L.G., Xu, C.L., Kuang, H., 2018. Anal. Chem. 90 (8), 5414–5421.
Gnanasammandhan, M.K., Idris, N.M., Bansal, A., Huang, K., Zhang, Y., 2016. Nat. Protoc. 11 (4), 688–713.
Gootenberg, J.S., Abudayyeh, O.O., Kellner, M.J., Joung, J., Collins, J.J., Zhang, F., 2018. Science 360 (6387), 439–444.
Guo, H., Li, Z.Q., Qian, H.S., Hu, Y., Muhammad, I.N., 2010. Nanotechnology 21 (12), 125602.
Hong, S.N., Zhang, X.T., Lake, R.J., Pawel, G.T., Guo, Z.J., Pei, R.J., Lu, Y., 2020. Chem. Sci. 11 (3), 713–720.
Hou, J., Zhang, H.C., Yang, Q., Li, M.Z., Song, Y.L., Jiang, L., 2014. Angew. Chem. Int. Ed. 53 (23), 5791–5795.
Hu, M.L., Yuan, C.Q., Tian, T., Wang, X.S., Sun, J., Xiong, E.H., Zhou, X.M., 2020. J. Am. Chem. Soc. 142 (16), 7506–7513.
Jinek, M., Chylinski, K., Fonfara, I., Hauer, M., Doudna, J.A., Charpentier, E., 2012. Science 337 (6096), 816–821.
Kovacs, L., Robertson, G.L., 1992. Bailliere Clin Endoc 6 (1), 107–127.

Li, C.Y., Cao, D., Qi, C.B., Kang, Y.F., Song, C.Y., Xu, D.D., Zheng, B., Pang, D.W., Tang, H.W., 2018. Anal. Chem. 90 (4), 2639–2647.
Li, C.Y., Kang, Y.F., Qi, C.B., Zheng, B., Zheng, M.Q., Song, C.Y., Guo, Z.Z., Lin, Y., Pang, D.W., Tang, H.W., 2019a. Anal. Chem. 91 (12), 7950–7957.
Li, C.Y., Zheng, B., Kang, Y.F., Tang, H.W., Pang, D.W., 2020a. ACS Sens. 5 (1), 199–207.
Li, Q., Zhou, S.H., Zhang, T., Zheng, B., Tang, H.W., 2020b. Biosens. Bioelectron. 150, 111866.
Li, Y., Teng, X.C., Zhang, K.X., Deng, R.J., Li, J.H., 2019b. Anal. Chem. 91 (6), 3989–3996.
Megahed, A.A., Hiew, M., Grunberg, W., Trefz, F.M., Constable, P.D., 2019. J. Dairy Sci. 102 (8), 7435–7444.
Min, K., Choi, S., Choi, Y., Jeon, H., 2014. Nanoscale 6 (23), 14531–14537.
Muhr, V., Wurth, C., Kraft, M., Buchner, M., Baeumner, A.J., Resch-Genger, U., Hirsch, T., 2017. Anal. Chem. 89 (9), 4868–4874.
Palermo, G., Ricci, C.G., Fernando, A., Basak, R., Jinek, M., Rivalta, I., Batista, V.S., McCammon, J.A., 2017. J. Am. Chem. Soc. 139 (45), 16028–16031.
Pardee, K., Green, A.A., Takahashi, M.K., Braff, D., Lambert, G., Lee, J.W., Ferrante, T., Ma, D., Donghia, N., Fan, M., Daringer, N.M., Bosch, I., Dudley, D.M., O'Connor, D. H., Gehrke, L., Collins, J.J., 2016. Cell 165 (5), 1255–1266.
Potyrailo, R.A., Bonam, R.K., Hartley, J.G., Starkey, T.A., Vukusic, P., Vasudev, M., Bunning, T., Naik, R.R., Tang, Z.X., Palacios, M.A., Larsen, M., Le Tarte, L.A., Grande, J.C., Zhong, S., Deng, T., 2015. Nat. Commun. 6, 7959.
Qu, H., Wang, L., Liu, J., Zheng, L., 2018. ACS Sens. 3 (10), 2071–2078.
Ratajczak, K., Lukasiak, A., Grel, H., Dworakowska, B., Jakiela, S., Stobiecka, M., 2019. Anal. Bioanal. Chem. 411 (26), 6899–6911.
Sedlmeier, A., Gorris, H.H., 2015. Chem. Soc. Rev. 44 (6), 1526–1560.
Shan, Y.Y., Zhou, X.M., Huang, R., Xing, D., 2019. Anal. Chem. 91 (8), 5278–5285.
Simpson, F.O., 1988. Lancet 2 (8601), 25–29.
Tsujimoto, Y., 1997. Cell Death Differ. 4 (6), 429–434.
Wang, D.D., Qi, G.H., Zhou, Y., Zhang, Y., Wang, B., Hu, P., Jin, Y.D., 2020. Chem. Commun. 56 (10), 1561–1564.
Wang, G., Fu, Y.K., Ren, Z.H., Huang, J., Best, S., Li, X., Han, G.R., 2018. Chem. Commun. 54 (49), 6324–6327.
Wang, Y.Q., Li, Z.H., Lin, Q.S., Wei, Y.R., Wang, J., Li, Y.X., Yang, R.H., Yuan, Q., 2019. ACS Sens. 4 (8), 2124–2130.
Wen, S.H., Zhou, J.J., Zheng, K.Z., Bednarkiewicz, A., Liu, X.G., Jin, D.Y., 2018. Nat. Commun. 9, 2415.
Xiong, Y., Zhang, J.J., Yang, Z.L., Mou, Q.B., Ma, Y., Xiong, Y.H., Lu, Y., 2020. J. Am. Chem. Soc. 142 (1), 207–213.
Yao, Q., Wang, Y.Q., Wang, J., Chen, S.M., Liu, H.Y., Jiang, Z.R., Zhang, X.E., Liu, S.M., Yuan, Q., Zhou, X., 2018. ACS Nano 12 (7), 6777–6783.
Zhang, Z.M., Shikha, S., Liu, J.L., Zhang, J., Mei, Q.S., Zhang, Y., 2019. Anal. Chem. 91 (1), 548–568.
Zhao, Y.J., Xie, Z.Y., Gu, H.C., Zhu, C., Gu, Z.Z., 2012. Chem. Soc. Rev. 41 (8), 3297–3317.